High-Performance Zinc Anode Enabled by Zincophilic and Hydrophobic ZnO@Nitrogen-Doped Carbon/MXene Interface

Yue Wang,[a] Qizhen Zhu,*[a] Yanze Li,[a] Yuan Ju,[a] Yong Yang,[a] and Bin Xu*[a, b]

Aqueous zinc-ion batteries (AZIBs) are one of the most promising systems for large-scale energy storage, but their zinc metal anodes suffer from unsatisfactory stability and reversibility due to the uncontrollable Zn dendrite growth and undesirable side reactions. Herein, a ZnO-anchored nitrogen-doped carbon/$Ti_3C_2T_x$ MXene composite (ZnO@NC/MXene) is developed as a protective layer onto the zinc anode, which establishes a zincophilic and hydrophobic interface. In the ZnO@NC/MXene layer, the nitrogen sites efficiently enhances the adsorption of Zn^{2+}, the ZnO provides homogenous nucleation sites for Zn^{2+} deposition, and the highly conductive MXene ensures even electric field distribution, synergistically inhibiting the zinc dendrites. Additionally, the hydrophobic ZnO@NC/MXene layer suppresses side reactions by limiting contact between the Zn anode and active water. Therefore, the Zn electrode modified by the ZnO@NC/MXene layer shows remarkable stability with a cycle life of over 2600 h in Zn‖Zn symmetric cell and outstanding reversibility with an average coulombic efficiency of 99.37% for over 1000 cycles in Zn‖Cu asymmetric cell. Coupled with V_2O_5 cathode, the full cell reveals excellent cycle stability of exceeding 1000 cycles at 4 A g^{-1}. These results indicate the potential of the zincophilic and hydrophobic ZnO@NC/MXene as a promising interface layer for protecting Zn anode in AZIBs.

Introduction

The increasing demand for energy storage devices against the backdrop of limited lithium resources has driven researchers to explore alternatives to lithium-ion batteries.[1,2] Aqueous zinc-ion batteries (AZIBs) have emerged as promising candidates due to their zinc metal anodes with abundant resources, high theoretical capacity (820 mAh g^{-1}) and low redox potential (−0.76 V vs. SHE).[3,4] However, the Zn anode suffers from several problems that limit its cycle life. Because of the uneven electric field distribution on the surface during Zn^{2+} deposition/stripping, the local current density is increased, leading to the formation of Zn dendrites, i.e., a phenomenon known as the "tip effect".[5,6] Moreover, in aqueous electrolytes, the Zn anode is susceptible to side reactions such as hydrogen evolution reaction (HER) and corrosion.[7–9] These issues lead to poor electrochemical cycle stability and reversibility of the Zn anode, posing major obstacles to the progress of AZIB development.

To address these challenges, various strategies have been proposed, such as the structural regulation of the zinc anode,[10,11] the electrolyte modification,[12–14] and the interface optimization.[15,16] Among these strategies, constructing an artificial protective layer at the interface between Zn anode and electrolyte stands out as a simple and effective approach. The zincophilic interface is conducive to inducing the uniform deposition of Zn^{2+} and inhibiting the formation of zinc dendrites, while the hydrophobic interface is beneficial for suppressing the side reactions like HER.[17] Therefore, the artificial layer with zincophilic and hydrophobic properties can significantly enhance the electrochemical stability and reversibility of Zn anode in AZIBs.

Various materials have been explored as interface layers for Zn anodes, including carbons,[18–20] metal oxides,[21,22] polymers,[23] and 2D transition metal carbide/nitride (MXene),[24–26] etc. The nitrogen-doped carbon layers can induce homogenous Zn^{2+} deposition due to their massive zincophilic sites and uniform electric field distribution, but their ability to transport Zn^{2+} is comparatively weak.[27–29] Metal oxides with high ionic conductivity offer an alternative for facilitating rapid Zn^{2+} transport, while their poor electronic conductivity may hinder the charge transfer at the interface.[30,31] Recently, metal oxide/carbon composites derived from MOF materials have garnered attention as interface layers for Zn anodes, which retain the skeleton structure of the precursor MOF materials and integrate the benefits of metal oxides and carbon materials, thereby providing superior protection for Zn anodes.[21,32,33] For instance, Xu et al.[34] synthesized the MOF-derived TiO_2/nitrogen-doped carbon composite and applied it onto Zn anode as

[a] Y. Wang, Dr. Q. Zhu, Y. Li, Y. Ju, Y. Yang, Prof. B. Xu
     State Key Laboratory of Organic–Inorganic Composites
     Beijing Key Laboratory of Electrochemical Process and Technology for
     Materials
     Beijing University of Chemical Technology
     Beijing 100029, China
     E-mail: zhuqz@mail.buct.edu.cn
             xubin@mail.buct.edu.cn
[b] Prof. B. Xu
     Shaanxi Key Laboratory of Chemical Reaction Engineering
     School of Chemistry and Chemical Engineering
     Yan'an University
     Yan'an 716000, China
     E-mail: xubin@yau.edu.cn

📱 Supporting information for this article is available on the WWW under
     https://doi.org/10.1002/batt.202400309

Batteries & Supercaps

Research Article
doi.org/10.1002/batt.202400309

Chemistry Europe
European Chemical
Societies Publishing

an interface layer. This composite layer exploited the strong interaction between TiO_2 and Zn^{2+} ions, along with the high conductivity of nitrogen-doped carbon, to synergistically inhibit Zn dendrite growth and HER, which endowed the zinc anode with a coulombic efficiency (CE) of 99.4% for 500 cycles at $2\,mA\,cm^{-2}$ and $1\,mAh\,cm^{-2}$. However, the MOF-derived composites typically consist of nano-particles that tend to aggregate, resulting in inadequate exposure of the zincophilic sites.

MXene materials with 2D morphology and tunable surface terminations offer distinct advantages as interface layers on Zn anode, including high lattice matching with zinc deposits, abundant zincophilic sites, excellent electronic conductivity, and good mechanical property.[17,24–26] Zhu et al.[25] constructed a tetramethylamine-intercalated $Ti_3C_2T_x$ MXene onto the Zn anode as an interface layer via an in-situ self-assembly method. This MXene-based layer redistributed the interface electric field and guided uniform and rapid Zn^{2+} deposition, enabling the Zn anode to exhibit stable cycle for 3600 h at $2\,mA\,cm^{-2}$ and $2\,mAh\,cm^{-2}$. Nevertheless, it's important to note that the abundant oxygen-containing terminations on MXene nanosheets may enhance the accumulation of active water molecules on Zn anodes, potentially exacerbating side reactions like HER and corrosion.

Herein, a ZnO-anchored nitrogen-doped carbon/$Ti_3C_2T_x$ MXene composite (ZnO@NC/MXene) was prepared by calcining a ZIF-8/MXene composite and constructed onto the Zn anode as a zincophilic and hydrophobic interface layer. Within the ZnO@NC/MXene layer, the doped nitrogen atoms in carbon serve as zincophilic sites, which are beneficial for capturing Zn^{2+} and de-solvating $[Zn(H_2O)_6]^{2+}$ ions, thereby reducing the interface concentration gradient. Additionally, the ZnO provides nucleation sites for Zn^{2+} and lowers the nucleation barrier, in favor of enhancing the deposition kinetics. The MXene nanosheets act as a conductive substrate, promoting uniform electric field distribution and preventing the agglomeration of the ZnO@NC nanoparticles, thereby ensuring the uniform distribution of zincophilic and nucleation sites. Furthermore, the hydrophobic property of the ZnO@NC/MXene layer reduces the contact between the Zn anode and active water, effectively limiting the side reactions at the Zn anode/electrolyte interface. As a result, the symmetric cell assembled with Zn electrodes with ZnO@NC/MXene layer exhibits outstanding stability with a cycle life of over 2600 h at $1\,mA\,cm^{-2}$ and $1\,mAh\,cm^{-2}$. The ZnO@NC/MXene-modified Zn||Cu asymmetric cell presents an average CE of 99.37% for over 1000 cycles at $5\,mA\,cm^{-2}$ and $1\,mAh\,cm^{-2}$. Besides, the full cell coupled with V_2O_5 cathode delivers good electrochemical performance with a capacity retention of 71.1% after 1000 cycles at a high current density of $4\,A\,g^{-1}$.

Experimental Section

Synthesis of $Ti_3C_2T_x$ MXene: Firstly, 0.99 g LiF (Alfa Aesar, 98.5%) was added to 10 mL HCl (12 M) and stirred evenly to form a HF etching environment.[35] Subsequently, 1.0 g Ti_3AlC_2 (11 Technology Co., Ltd.) was gradually added to the prepared etching solution under magnetic stirring. The mixture was stirred at 35°C for 24 h to ensure complete etching of the Al atomic layers in Ti_3AlC_2. The resulting multilayer $Ti_3C_2T_x$ clay was then repeatedly centrifuged and washed with deionized water until the pH of the supernatant reached neutral. Monolayer MXene nanosheets dispersion was obtained by repeated ultrasonic stripping (under an inert atmosphere) and centrifugation to collect the supernatant.

Synthesis of ZnO@NC/MXene: To prepare solution A, 1.5 g Zn-$(NO_3)_2 \cdot 6H_2O$ was dissolved in 90 mL methanol, while solution B was prepared by dissolving 3.3 g 2-methylimidazole in 90 mL methanol. Solution A was added to $Ti_3C_2T_x$ aqueous dispersion ($3\,mg\,mL^{-1}$) and thoroughly stirred to ensure full anchoring of Zn^{2+} on the surface of $Ti_3C_2T_x$ sheets. Subsequently, solution B was poured into the mixture and stirred at 550 rpm for 24 h. Then, the product was collected by vacuum filtration and washed with methanol three times to remove excess Zn^{2+}. The resulting ZIF-8/MXene composite was then calcined at 600°C in an Ar atmosphere for 2 h to obtain ZnO@NC/MXene composite material.

Preparation of Zn electrode with ZnO@NC/MXene layer: The zinc foil with a thickness of 100 μm was used as Zn electrode. ZnO@NC/MXene and polyvinylidene difluoride in a mass ratio of 95:5 were thoroughly ground in N,N dimethylpyrrolidone solvent to form a slurry, which was then coated on the Zn electrode by scraping and dried in an oven at 60°C for 10 h. The obtained material was then stamped into electrodes with a diameter of 10 mm. For comparison, the Zn electrode with $Ti_3C_2T_x$ MXene layer was also prepared by coating the freeze-dried $Ti_3C_2T_x$ MXene powder onto Zn electrode via the consistent method.

Preparation of V_2O_5 cathode: V_2O_5 cathode was prepared by mixing V_2O_5 (Thermo Scientific), Super P carbon black, and polyvinylidene difluoride in a mass ratio of 7:2:1 in N,N dimethylpyrrolidone solvent to prepare a slurry. The slurry was coated on stainless steel mesh discs with diameters of 10 mm and dried in an oven at 120°C for 10 h to obtain V_2O_5 cathode. The areal loading of V_2O_5 on each cathode was controlled at 1–$2\,mg\,cm^{-2}$.

Material Characterizations: The morphologies of the materials and the electrodes were examined using scanning electron microscopy (SEM, S-4700, Hitachi) and transmission electron microscope (TEM, Hitachi HT7700). For analyzing the composition of the composites, X-ray diffraction (XRD) patterns were obtained using a Bruker D8 Avance X-ray diffractometer, and X-ray photoelectron spectroscopy (XPS) were conducted on a ESCALAB 250 spectrometer with Cu Kα radiation. The graphitization degree of the nitrogen-doped carbon was studied by Raman spectroscopy (Invia Reflex). Thermal gravimetric analysis (TGA) was performed on a Mettler Toledo thermal gravimetric analyzer under N_2 atmosphere from room temperature to 1000°C at a heating rate of $5°C\,min^{-1}$. The wettability of different electrodes with 2 M $ZnSO_4$ electrolyte was investigated by a contact angle tester (JGW-360B). In-situ optical microscopy was used to investigate the morphology evolution of the Zn electrode during zinc deposition. Atomic force microscopy (AFM, DMFASTSCAN2-SYS) was employed to observe the surface roughness changes of the electrodes under different deposition capacities.

Electrochemical Measurements: The Tafel plots of different electrodes were obtained within a three-electrode system in a potential range of −0.9 V to −1.1 V (vs. Ag/AgCl) at a scan rate of $2\,mV\,s^{-1}$ using 2 M $ZnSO_4$ as the electrolyte, the coated Zn foil as working electrode, platinum electrode as counter electrode, and Ag/AgCl electrode as reference electrode. HER behavior on these electrodes was assessed by linear scanning voltammetry (LSV) test in 1 M Na_2SO_4 electrolyte with the Hg/HgO electrode as reference electrode in a potential range from −1.4 V to −2.0 V (vs. Hg/HgO)

Batteries & Supercaps

Research Article
doi.org/10.1002/batt.202400309

Chemistry
Europe

European Chemical
Societies Publishing

at $1\,mV\,s^{-1}$. The ionic conductivity of the ZnO@NC/MXene layer was studied via electrochemical impedance spectroscopy (EIS) of a ZnO@NC/MXene-modified Ti symmetrical cell over the frequency range of $10^{-2}\sim10^{5}\,Hz$ using a CHI760D electrochemical workstation.[36] The Zn^{2+} transference numbers ($t_{Zn^{2+}}$) were calculated based on the EIS curves before and after chronoamperometry (CA) test for 3000 s by the following equation:[37]

$$t_{Zn^{2+}} = \frac{\frac{\nabla V}{I_0} - R_0}{\frac{\nabla V}{I_{ss}} - R_{ss}} \tag{1}$$

where I_0 and R_0 are the initial current of the CA test and the impedance of fresh symmetrial cells, ∇V is the voltage polarization applied (10 mV), I_{ss} and R_{ss} are the steady state current and impedance after CA test.

The performance of the Zn electrode with the ZnO@NC/MXene layer was evaluated through various configurations in the CR2032 cells, which were assembled in an air environment using 2 M $ZnSO_4$ electrolyte and glass fiber membrane (Whatman GF/D) separators. The symmetric cells comprised two identical electrodes as both cathodes and anodes. The asymmetric cells were assembled using ZnO@NC/MXene-modified Zn anodes and Cu cathodes. The full cells were constructed with ZnO@NC/MXene-modified Zn anodes, coupled with V_2O_5 cathodes. Cyclic voltammetry (CV) test of the cells was performed using a CHI760D electrochemical workstation. For the Zn‖Cu asymmetric cells, CV was conducted in a range of $-0.2\sim1.0\,V$ at a scan rate of $1\,mV\,s^{-1}$. For the Zn‖V_2O_5 full cells, CV was performed in a range of $0.3\sim1.5\,V$ at a scan rate of $0.1\,mV\,s^{-1}$. Galvanostatic charge-discharge tests were conducted using a Land BT 2000 battery automatic tester (Wuhan, China). EIS was conducted from 100 kHz to 10 mHz with a potential amplitude of 10 mV.

Theoretical Calculations: The CASTEP module in Materials Studio was used for constructing the adsorption model, and the Perdew-Burke-Ernzerhof (PBE) formula in the generalized gradient approximation (GGA) was used for density functional theory (DFT) calculations. The valence electrons are considered by using the plane wave basis set with an energy cut-off of 310 eV. Geometric optimization and electron self-consistency were ensured when the force on each atom was below $0.01\,eV\,Å^{-1}$ and the energy change was less than $10^{-5}\,eV$. The Monkhorst–Pack method was utilized for selecting k-points in the Brillouin zone, set to $1\times5\times1$ for nitrogen-doped carbon, $3\times3\times1$ for $Ti_3C_2O_2$ (002), and $5\times5\times1$ for Zn (002). Weak interaction corrections between the Zn atom and nitrogen-doped carbon were handled using the TS DFT-D method. The adsorption energy ($\triangle E_a$) was calculated using the formula:[38]

$$\Delta E_a = (E_{total} - E_{sub} - E_{Zn}) \tag{2}$$

where E_{total}, E_{sub} and E_{Zn} denoted the energies of the Zn adsorbed on ZnO@NC/MXene, the pure ZnO@NC/MXene and the isolated Zn atom, respectively.

Results and Discussion

The ZnO@NC/MXene composite material was prepared by a simple in-situ grown of ZIF-8 MOF on the surface of the MXene nanosheets and followed calcination process. As the MXene nanosheets limit the excessive growth of ZIF-8 nanoparticles and prevent the agglomeration among the particles, the ZIF-8

loaded on the MXene nanosheets shows smaller particles and more uniform distribution, compared to that without MXene (Figure S1). In the subsequent calcination process under Ar atmosphere, the ZIF-8 particles were decomposed into ZnO-anchored nitrogen-doped carbon. The evolution process from ZIF-8/MXene to ZnO@NC/MXene with temperature increasing is illustrated by TGA curves (Figure S2). The weight loss at $400\sim550\,°C$ is attributed to the carbonization of the organic ligands in ZIF-8 and the formation of the ZnO/C composite.

The SEM images depict the microstructure of the as-prepared ZnO@NC/MXene composite. As shown in Figure 1a, the composite retains the characteristic feature of MXene nanosheets. The elemental mapping in Figure 1b shows the uniform distribution of Ti, C, N and Zn elements in the composite (Figure S3). The TEM image confirms that nano-scale particles are uniformly loaded on the MXene nanosheets (Figure 1c). The lattice fringes of 0.28 nm and 0.26 nm in the high-resolution TEM (HRTEM) image (Figure 1d) correspond to the (100) and (002) crystal planes of ZnO, respectively, which prove the presence of ZnO nanoparticles on the MXene nanosheets.

The chemical composition of the ZnO@NC/MXene material was thoroughly characterized by XRD, XPS and Raman spectra. As shown in Figure 1e, the XRD of the ZIF-8/MXene composite reveals the characteristic peaks of ZIF-8, demonstrating the successful growth of ZIF-8 with good crystallinity on the MXene nanosheets. After calcination, two peaks at $6.9°$ and $60.3°$, related to MXene (002) and (110) crystal planes, respectively, are maintained, indicating that the calcined MXene retains its original composition. However, the characteristic peaks of ZIF-8 disappear, being replaced by a broad peak at $\sim25°$ attributed to amorphous carbon and a distinct peak at $34.4°$ corresponding to ZnO (002) crystal plane, confirming the transformation from ZIF-8/MXene to ZnO@NC/MXene by the calcination. The XPS spectrum of the ZnO@NC/MXene composite exhibits the presence of Zn, O, Ti, C, and N elements (Figure S4a). Compared to the O 1s spectrum of MXene (Figure S4b), a new peak at 530.94 eV appears in ZnO@NC/MXene (Figure 1f), which is attributed to Zn–O bonds of ZnO. In the Zn 2p XPS spectrum (Figure 1g), the binding energy difference of the spin-orbit splitting between Zn $2p_{3/2}$ (1021.8 eV) and Zn $2p_{1/2}$ (1044.9 eV) is 23.1 eV, further confirming the presence of ZnO.[39] Moreover, the N 1s spectrum in Figure 1h displays the peaks at 398.4 eV, 399.07 eV, and 400.1 eV, ascribed to pyridinic nitrogen (N-6), pyrrolic nitrogen (N-5) and graphitic N (N–Q), respectively, demonstrating the formation of N-doped carbon in the ZnO@NC/MXene composite. Besides, the Ti 2p peaks in both the MXene and the ZnO@NC/MXene composite (Figure S4c) are consistent with those of the previously reported $Ti_3C_2T_x$ MXene,[40] suggesting the stability of the composition and structure of $Ti_3C_2T_x$ MXene after calcination. The Raman spectrum was utilized to investigate the carbon form in the ZnO@NC/MXene composite, in which the D-band ($1350\,cm^{-1}$) and G-band ($1580\,cm^{-1}$) represent the A_{1g} vibration mode of the disordered sp^3 carbon defect and the E_{2g} vibration mode of the sp^2 hybrid carbon atom, respectively.[41] The high ratio of D-

Batteries & Supercaps

Research Article
doi.org/10.1002/batt.202400309

Chemistry
Europe
European Chemical
Societies Publishing

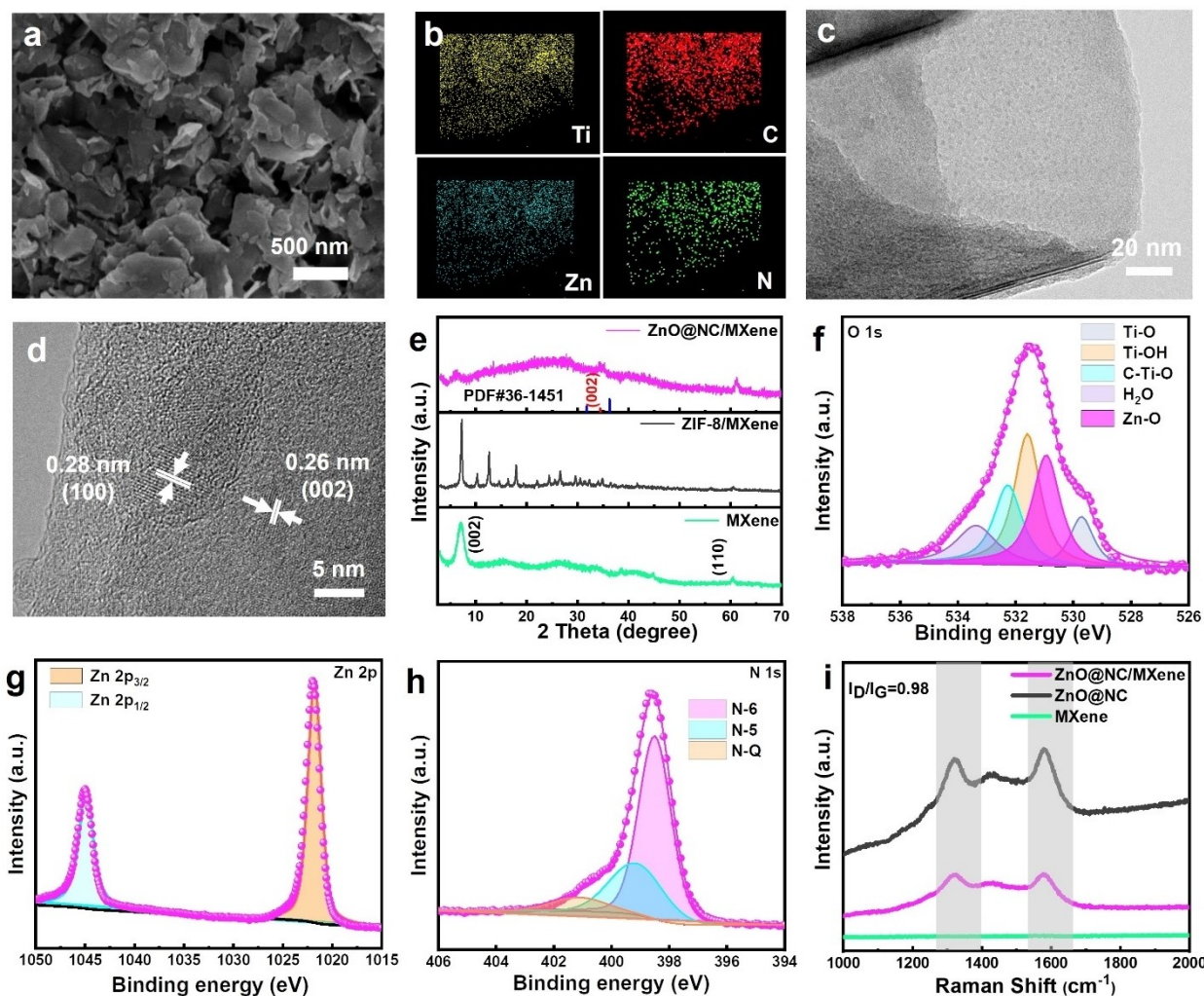**Figure 1.** (a) SEM image, (b) EDS mapping, (c) TEM image, and (d) HRTEM image of ZnO@NC/MXene composite. (e) XRD patterns of $Ti_3C_2T_x$ MXene, ZIF-8/MXene and ZnO@NC/MXene. High-resolution XPS spectra of (f) O 1s, (g) Zn 2p and (h) N 1s of ZnO@NC/MXene composite. (i) Raman patterns of $Ti_3C_2T_x$ MXene, ZnO@NC and ZnO@NC/MXene.

band to G-band in the ZnO@NC/MXene indicates the significant nitrogen doping in the carbon (Figure 1i).

The ZnO@NC/MXene (or pure MXene) interface layer was constructed on the Zn electrode by a simple scraping method. The SEM image (Figure 2a) shows that the ZnO@NC/MXene layer with a thickness of ~11.12 μm is uniformly and densely bonded on the Zn electrode. As shown in Figure 2b and Figure S5a, the $Ti_3C_2T_x$ MXene layer enhances the electrolyte's wettability to the Zn electrode with the decreased contact angle from 89.1° to 55.3°, due to the oxygen-containing terminations on the MXene surface. In contrast, the ZnO@NC/MXene layer is hydrophobic, resulting in an increased contact angle of 133.9°, which can be ascribed to the removal of some terminations on the MXene during the calcination treatment and the introduction of hydrophobic ZnO@NC (Figure S5b). The construction of the hydrophobic interface layer effectively prevents direct contact between the Zn electrode and active water molecules in the electrolyte, beneficial for mitigating the side reactions such as HER and corrosion.[42]

In order to investigate the influence of the interface layer on the adsorption behavior of Zn^{2+}, the adsorption energies of Zn^{2+} on nitrogen-doped carbons (pyrrolic N, pyridinic N, and graphitic N), $Ti_3C_2O_2$ MXene (002) and Zn (002) crystal planes were elucidated by DFT calculation. The results in Figure S6 and S7 indicate that the adsorption energy of $Ti_3C_2O_2$ MXene (002) crystal plane with Zn^{2+} (−1.14 eV) is much larger than that of Zn (002) crystal plane (−0.67 eV), as the oxygen-containing terminations on the MXene act as electron-rich Lewis bases to form strong interactions with the electron-deficient Zn^{2+}. Moreover, pyridine nitrogen-doped carbon (−3.67 eV) (Figure S6c) and pyrrole nitrogen-doped carbon (−5.26 eV) (Figure 2c) exhibit larger adsorption energy with Zn^{2+}. It means that despite the removal of −O terminations during the calcination process, the −N sites with stronger Zn^{2+} capture ability are introduced. Furthermore, the nitrogen sites of pyridine and pyrrole in nitrogen-doped carbon can significantly extend the bond length between Zn^{2+} and surrounding solvation water molecules, leading to the distortion of the $[Zn(H_2O)_6]^{2+}$

Batteries & Supercaps

Research Article
doi.org/10.1002/batt.202400309

Chemistry Europe
European Chemical
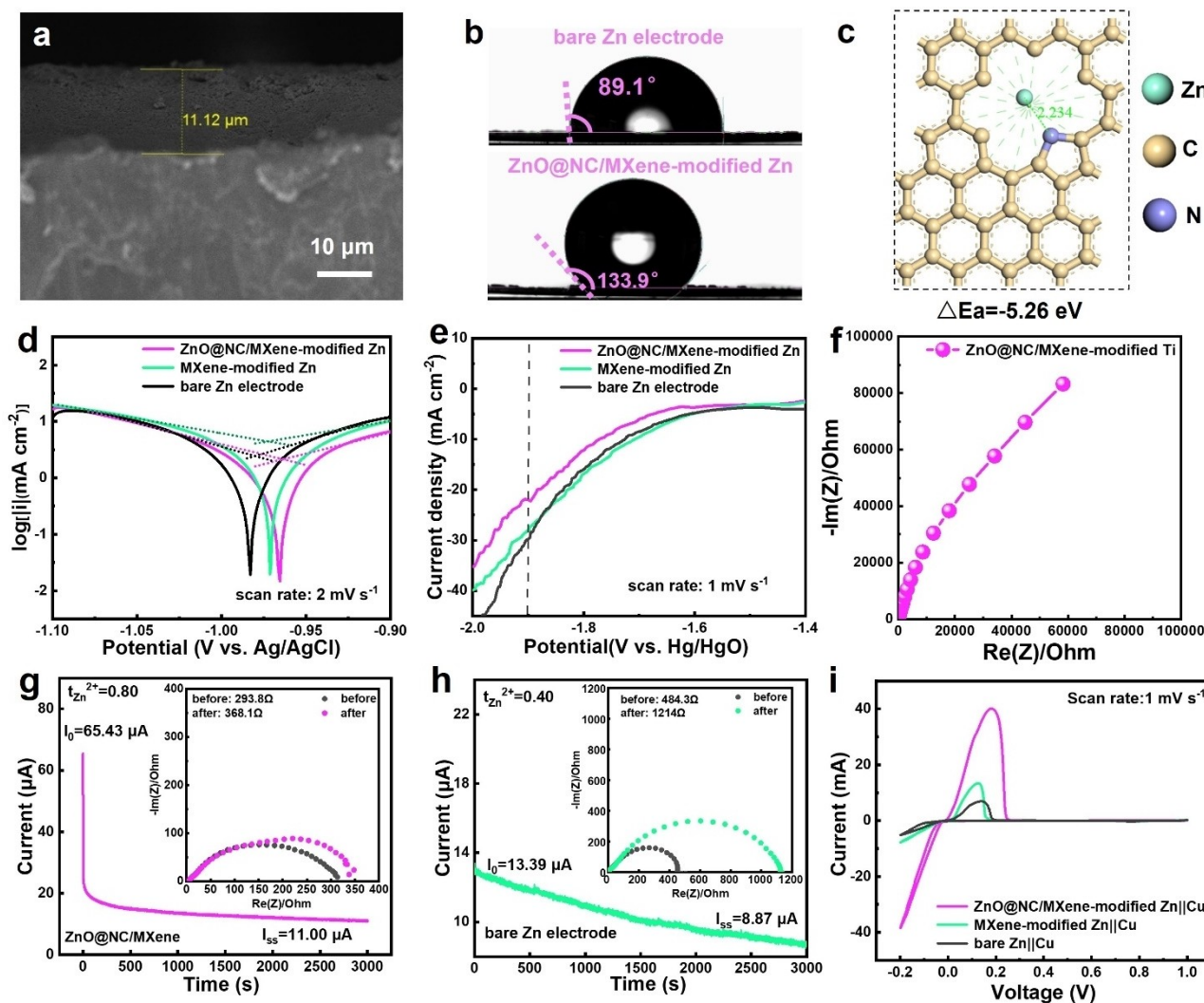Societies Publishing

Figure 2. (a) Cross-sectional SEM image of ZnO@NC/MXene-modified Zn electrode. (b) Contact angles of 2 M $ZnSO_4$ electrolyte on bare Zn and ZnO@NC/MXene-modified Zn electrodes. (c) Adsorption model and the corresponding energy of Zn^{2+} captured in pyrrolic N-doped carbon. (d) Tafel and (e) LSV curves of ZnO@NC/MXene-modified Zn, MXene-modified Zn and bare Zn electrodes. (f) Nyquist plots of Ti||Ti symmetric cell with ZnO@NC/MXene layer. CA curves of Zn||Zn symmetric cells with (g) ZnO@NC/MXene-modified Zn and (h) bare Zn electrodes at an overpotential of 10 mV for 3000 s with the EIS spectra before and after the CA test in the inset. (i) CV curves of Zn||Cu asymmetric cells based on ZnO@NC/MXene-modified Zn, MXene-modified Zn and bare Zn electrodes.

solvation structure and thereby promoting the de-solvation process.

To explore the influence of the ZnO@NC/MXene layer on HER and corrosion reactions at the interface, linear polarization and LSV tests were conducted. Tafel plots in Figure 2d show that the ZnO@NC/MXene layer enhances the Zn electrode's corrosion potential (-0.964 V) and reduces its corrosion current density ($2.15\ \mathrm{mA\,cm^{-2}}$), indicating enhanced corrosion resistance and decreased corrosion rate. In LSV curves (Figure 2e), at 1.9 V (vs. Hg/HgO), the current density of HER decreases from $29.69\ \mathrm{mA\,cm^{-2}}$ for bare Zn to $27.94\ \mathrm{mA\,cm^{-2}}$ for the MXene-modified Zn electrode, and further to $21.98\ \mathrm{mA\,cm^{-2}}$ for the ZnO@NC/MXene-modified Zn electrode, demonstrating the efficient mitigation of HER by the ZnO@NC/MXene layer. The suppression of the side reactions is ascribed to the hydrophobic property of the ZnO@NC/MXene layer, which decreases the

direct contact between the Zn anode and active water molecules at the interface.

The ZnO@NC/MXene layer shows a high ionic conductivity of $9.18\ \mathrm{mS\,cm^{-1}}$, as determined from the fitted EIS spectrum in Figure 2f with the equivalent circuit (Figure S8), ensuring fast Zn^{2+} transport through the interface layer. Furthermore, the migration number of Zn^{2+} ions ($t_{Zn^{2+}}$) in the symmetrical cell with ZnO@NC/MXene-modified Zn electrodes was calculated to be 0.80 (Figure 2g), significantly higher than that in the cell with bare Zn (Figure 2h). The notable increase means that the ZnO@NC/MXene layer effectively alleviates the concentration gradient of Zn^{2+} ions and inhibits the formation of zinc dendrites. In addition, CV measurements were performed on Zn||Cu asymmetric cells with and without the interface layers at a scan rate of $1\ \mathrm{mV\,s^{-1}}$ to assess the effect of the ZnO@NC/MXene layer on zinc deposition/stripping behavior. As shown in

Figure 2i, the ZnO@NC/MXene-modified Zn electrode delivers the lowest nucleation overpotential and the highest response current intensity compared to the MXene-modified Zn and bare Zn electrodes, suggesting superior reaction kinetics. It is attributed to the ZnO as nucleation sites that reduce the nucleation barrier, and the highly conductive MXene that facilitates uniform electric field distribution.

The morphology evolution during Zn^{2+} deposition on ZnO@NC/MXene-modified Zn and bare Zn electrodes was observed using in-situ optical microscopy to investigate the inhibition of zinc dendrites and side reactions by the interface layer. The bare Zn electrode shows a smooth and flat surface in Figure S9. After 20 min of deposition at a current density of 5 mA cm^{-2}, small protrusions emerge on the Zn electrode surface with the tips exhibiting higher electric field strength, which further induce the deposition of Zn^{2+} at their tips. Upon reaching a deposition time of 40 min, the protrusions evolve into large dendrites with hydrogen bubbles adsorbed on the electrode surface. In contrast, the Zn electrode with the ZnO@NC/MXene layer reveals uniform deposition morphology (Figure 3a). As the deposition capacity increases, no significant change is observed on the surface of the ZnO@NC/MXene-

modified electrode, indicating uniform deposition of Zn^{2+} under the protection of the interface layer. Even after 40 min of deposition, the epitaxial deposition of Zn on the surface of the protective layer is still uniform without obvious dendrite.

SEM and AFM were also employed to investigate the morphology evolution of deposited zinc on the Zn electrodes, providing deeper insights into the Zn dendrite growth process. As depicted in Figure 3b, the bare Zn electrode shows Zn dendrites at a deposition capacity of 5 mAh cm^{-2}, and experiences surface damage characterized by corrosion pits and dendrites with a deposition of 30 mAh cm^{-2} (Figure 3c). Conversely, for the ZnO@NC/MXene-modified Zn electrode, with the deposition capacity increasing, the gaps of the ZnO@NC/MXene layer are gradually filled with the deposited Zn, as indicated by the area selected by the pink box in Figure 3d. Even at a high capacity of 30 mAh cm^{-2}, the Zn deposition remains remarkably smooth without dendrite formation (Figure 3e). The AFM test at the same deposition capacities further confirms this observation. With the Zn deposition, the bare Zn electrode exhibits increased fluctuations in the surface height (Figure 3f, g and Figure S10), whereas the ZnO@NC/MXene-modified Zn electrode shows a gradual flattening of its surface
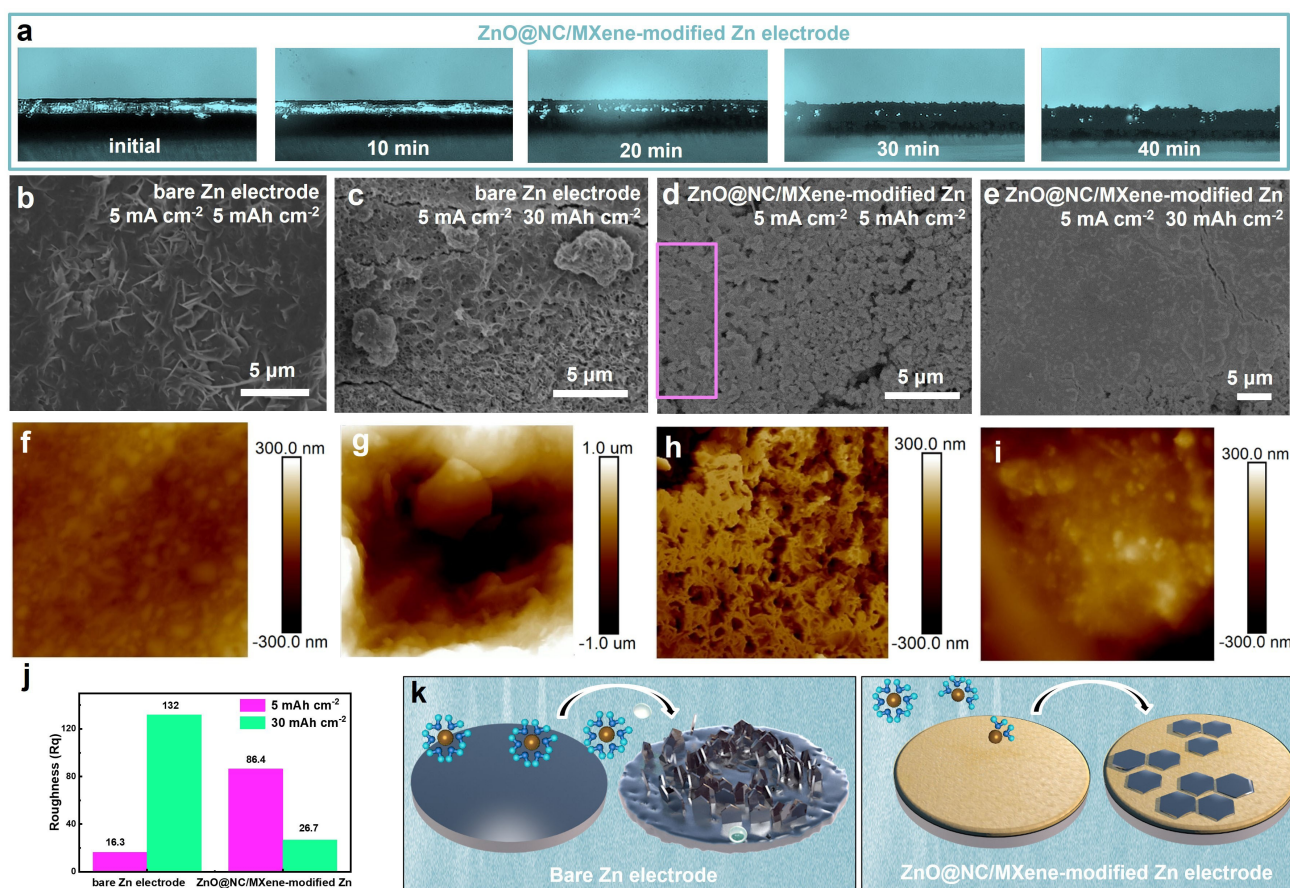

Figure 3. (a) In-situ optical microscopy images of ZnO@NC/MXene-modified Zn electrode during zinc deposition at 5 mA cm^{-2}. SEM images of the electrodes with different deposition capacities: bare Zn electrodes with capacities of (b) 5 mAh cm^{-2} and (c) 30 mAh cm^{-2}; ZnO@NC/MXene-modified Zn electrodes with capacities of (d) 5 mAh cm^{-2} and (e) 30 mAh cm^{-2}. AFM images of the electrodes with different deposition capacities: bare Zn electrodes with capacities of (f) 5 mAh cm^{-2} and (g) 30 mAh cm^{-2}; ZnO@NC/MXene-modified Zn electrodes with capacities of (h) 5 mAh cm^{-2} and (i) 30 mAh cm^{-2}. (j) Roughness of bare Zn and ZnO@NC/MXene-modified Zn electrodes at 5 mAh cm^{-2} and 30 mAh cm^{-2}. (k) Schematic of zinc deposition morphology on bare Zn and ZnO@NC/MXene-modified Zn electrodes.

(Figure 3h, i and Figure S11). Figure 3j illustrates the surface roughness of the electrodes under various deposition capacities. Notably, as the deposition capacity increases, the surface roughness of the bare Zn electrode increases, while that of the ZnO@NC/MXene-modified Zn electrode decreases.

The mechanism of the ZnO@NC/MXene layer for protecting the Zn electrode is schematically illustrated in Figure 3k. In the case of bare Zn electrode, the lack of nucleation sites and uneven electric field distribution on the surface lead Zn^{2+} ions to preferentially deposit on the protrusions, causing a "tip effect." In addition, the dendrites exacerbate side reactions like HER and corrosion by exposing fresh Zn surfaces. In contrast, the ZnO@NC/MXene-modified electrode benefits from strong Zn^{2+} adsorption by highly zincophilic -N sites in carbon and uniformly distributed nucleation sites of ZnO. Moreover, MXene nanosheets act as a conductive substrate, ensuring full exposure of active sites and even electric field distribution on the electrode. Consequently, the synergistic components of ZnO, nitrogen-doped carbon, and MXene ensure homogeneous Zn^{2+} concentration and uniform Zn^{2+} deposition with fast kinetics. Additionally, the hydrophobic property of the layer limits side reactions at the interface, allowing the Zn electrode to maintain a smooth and flat surface even after high-capacity plating.

The aforementioned studies initially investigated the effectiveness of the ZnO@NC/MXene composite layer in inducing uniform Zn^{2+} deposition and suppressing side reactions. Furthermore, Zn||Zn symmetrical cells and Zn||Cu asymmetrical cells were assembled to explore the practical application potential of the ZnO@NC/MXene interface layer. As shown in Figure 4a, at 1 mA cm^{-2} and 1 mAh cm^{-2}, the symmetrical cell utilizing bare Zn electrodes fails after 94 h of cycling, whereas the incorporation of the MXene layer extends the cycle life to 351 h. Furthermore, the symmetric cell employing Zn electrodes with the ZnO@NC/MXene layer exhibits remarkable cycle stability with low voltage hysteresis (~34 mV) for over 2600 h, indicating that the ZnO@NC/MXene interface layer significantly enhances the stability of Zn electrode during zinc deposition/stripping and reduces the nucleation barrier of Zn^{2+} ions. The ZnO@NC/MXene-modified symmetric cell also shows outstanding rate performance (Figure 4b). Even at a high current density of 5 mA cm^{-2}, its voltage hysteresis remains at ~65 mV, much lower than that of the cell with bare Zn (94 mV) and the $Ti_3C_2T_x$ MXene-modified Zn electrodes (74 mV), suggesting significantly improved kinetics. In Figure 4c, under a condition of 5 mAh cm^{-2} and 1 mAh cm^{-2}, the ZnO@NC/MXene-modified symmetric cell cycles stably for 736 h with a small voltage hysteresis. However, the symmetrical cell with bare Zn electrodes only operates for 209 h before experiencing a short circuit,
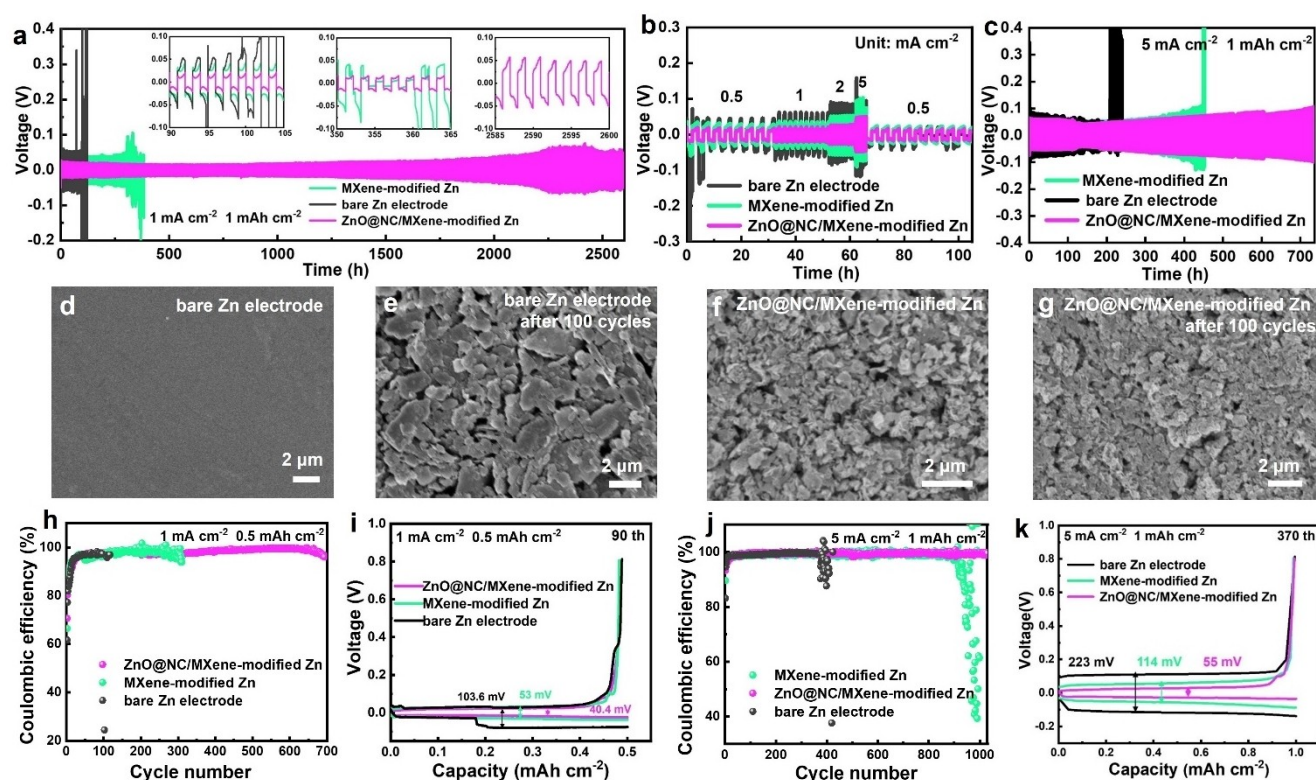

Figure 4. (a–c) Electrochemical performance of Zn||Zn symmetric cells based on bare Zn, $Ti_3C_2T_x$ MXene-modified Zn and ZnO@NC/MXene-modified Zn electrodes: (a) cycle performance at 1 mA cm^{-2} and 1 mAh cm^{-2}; (b) rate capability; (c) cycle performance at 5 mA cm^{-2} and 1 mAh cm^{-2}. SEM images of Zn electrodes before and after cycling: (d) fresh bare Zn; (e) bare Zn after 100 cycles; (f) fresh ZnO@NC/MXene-modified Zn electrode; (g) ZnO@NC/MXene-modified Zn electrode after 100 cycles. (h–k) Electrochemical performance of Zn||Cu asymmetrial cells based on bare Zn, $Ti_3C_2T_x$ MXene-modified Zn and ZnO@NC/MXene-modified Zn electrodes: (h) CE at 1 mA cm^{-2} and 0.5 mAh cm^{-2} and (i) the corresponding voltage curves at 90th cycle. (j) CE at 5 mA cm^{-2} and 1 mAh cm^{-2} and (k) the corresponding voltage curves at 370th cycle.

Batteries & Supercaps

Research Article
doi.org/10.1002/batt.202400309

Chemistry Europe
European Chemical
Societies Publishing

manifested by a sudden increase in voltage hysteresis (Figure S12). The MXene-modified symmetrical cell also shows a fluctuation after 450 h of cycling, signifying a short circuit (Figure S13). In contrast, the voltage hysteresis of the ZnO@NC/MXene-modified symmetric cell remains consistently stable after over 730 h (Figure S14). This result illustrates the advantage of the ZnO@NC/MXene layer in inhibiting the formation and growth of Zn dendrites even at high current density. Subsequently, the cycle stability of the symmetrical cells with and without the ZnO@NC/MXene layer was tested at a high depth of discharge (DOD). The ZnO@NC/MXene-modified symmetric cell displays a cycle life of over 200 h at the depth of discharge of ~48% (Figure S15), demonstrating that the ZnO@NC/MXene protective layer can also endow Zn electrode with a high utilization rate. Compared with the analogical studies on protective layers for Zn electrodes, the ZnO@NC/MXene layer in this work remarkably extends the cycle life of the Zn anode across various current densities and deposition capacities (Table S1), demonstrating its superior performance.[43,44]

The morphological evolution of the electrode surfaces before and after 100 cycles in symmetrial cells at a current density of 5 mA cm^{-2} and 1 mAh cm^{-2} was observed by SEM. Compared to the smooth surface of the fresh Zn electrode before cycling (Figure 4d), the bare Zn electrode exhibits the formation of numerous mossy dendrites and corrosion pits on the surface after 100 cycles (Figure 4e). Conversely, the morphology of the ZnO@NC/MXene-modified electrode after cycling shows minimal change with no observable dendrites, and the layer remains tightly combined with the Zn electrode (Figure 4f, g). It means that the ZnO@NC/MXene interface layer effectively protects the Zn anode from the formation and growth of Zn dendrites, which is attributed to the uniform electric field distribution guided by MXene and the even Zn^{2+} flux facilitated by the −N sites and ZnO within the layer.

Furthermore, the deposition/stripping efficiency of the Zn electrode with the ZnO@NC/MXene interface layer was analyzed by assessing the CE values of the Zn||Cu asymmetrical cells. Under conditions of 1 mA cm^{-2}, 0.5 mAh cm^{-2} and 0.8 V cut-off voltage, the cell with bare Zn can only operate for 97 cycles with an average CE of 95.05% (Figure 4h). The incorporation of the MXene interface layer prolongs the life of the Zn||Cu cell to 311 cycles with a CE of 97.04%. Moreover, the ZnO@NC/MXene-modified Zn||Cu cell delivers much improved electrochemical reversibility with stable charge and discharge for 700 cycles and an average CE of 97.94%. As depicted in the charge-discharge curves at the 90th cycle (Figure 4i), the voltage hysteresis of the ZnO@NC/MXene-modified Zn||Cu asymmetrical cell is much lower than that of the bare Zn||Cu and MXene-modified Zn||Cu cells. Also, in the charge-discharge curves at the 310th cycle (Figure S16), the ZnO@NC/MXene-modified Zn||Cu cell exhibits a smaller voltage hysteresis (36 mV) compared to the MXene-modified Zn||Cu cell (156 mV), suggesting that the composite layer not only significantly enhances the reversibility of zinc deposition/stripping but also efficiently decreases the electrochemical polarization. Moreover, when the current density is increased to

5 mA cm^{-2}, the superiority of the ZnO@NC/MXene protective layer becomes even more apparent. The ZnO@NC/MXene-modified Zn||Cu cell shows a cycle life of over 1000 cycles with a high CE of 99.37% (Figure 4j). In contrast, the bare Zn||Cu cell reveals fluctuating CE after 370 cycles, and the MXene-modified Zn||Cu cell fails after 914 cycles with an average CE of 99.24%. Consistently, the ZnO@NC/MXene-modified Zn||Cu cell demonstrates the lowest voltage hysteresis (55 mV) among the three cells (Figure 4k), further verifying the effective role of the ZnO@NC/MXene protective layer in improving the electrochemical kinetics. The high CE and extended cycle life of the ZnO@NC/MXene-modified Zn||Cu cell can be attributed to the hydrophobic interface layer that enhances the utilization of the zinc anode by suppressing side reactions and the synergistic effect of nitrogen adsorption sites and ZnO nucleation sites in the layer that facilitates highly reversible deposition/stripping kinetics.

V$_2$O$_5$ was selected as the cathode material to evaluate the performance of the ZnO@NC/MXene interface layer in full cells, wherein Zn^{2+} storage is achieved by Zn^{2+} extraction/insertion behavior accompanied by multiple valence transitions of vanadium.[32,45,46] The morphology of the used V$_2$O$_5$ is depicted in Figure S17a, which shows irregular particles in sub-micron size. Also, its high purity is confirmed by the XRD pattern in Figure S17b. The ZnO@NC/MXene-modified Zn anode (or bare Zn anode) was coupled with the V$_2$O$_5$ cathode for assembling the full cell. CV curves of the full cells are shown in Figure 5a. Compared with the bare Zn||V$_2$O$_5$ cell, the ZnO@NC/MXene-modified Zn||V$_2$O$_5$ cell shows a narrower gap between the redox peaks, confirming that the ZnO@NC/MXene interface layer is beneficial for achieving high reversibility and fast reaction kinetics of ZIBs.

After an activation process,[45–48] the ZnO@NC/MXene-modified Zn||V$_2$O$_5$ cell presents higher capacity than the cell without the interface layer at each current density, meaning the enhancement in rate performance (Figure 5b). At current densities of 1, 2, 3, and 4 A g^{-1}, its discharge capacities maintain 180.5, 169.6, 163.0, and 156.4 mAh g^{-1}, respectively. Upon returning to 1 A g^{-1}, the discharge capacity reverts to 177.6 mAh g^{-1}, significantly outperforming the full cell with bare Zn anode. The galvanostatic charge/discharge curves of the ZnO@NC/MXene-modified Zn||V$_2$O$_5$ cell at different current densities are shown in Figure 5c. Even at high current densities, the characteristic platforms are easily observed, indicating that the ZnO@NC/MXene layer benefits the improvement of charge transfer kinetics in ZIBs. In addition to enhancing the capacity and rate performance of ZIBs, the ZnO@NC/MXene-modified Zn||V$_2$O$_5$ cell achieves stable 1000 cycles with a capacity retention of 71.1% at 4 A g^{-1}, much superior to the bare Zn||V$_2$O$_5$ cell (Figure 5d). As illustrated in Figure 5e, the ZnO@NC/MXene-modified Zn||V$_2$O$_5$ cell also reveals smaller voltage hysteresis during the long-term cycle. Besides, the EIS spectrum of the ZnO@NC/MXene-modified Zn||V$_2$O$_5$ cell in Figure 5f reveals a small semicircle in high-frequency and mid-frequency regions, indicating a low interfacial charge transfer resistance (R$_{ct}$). Fitted with the equivalent circuit in the inset, the R$_{ct}$ value decreases from 105 Ω to 51 Ω upon the introduction of the
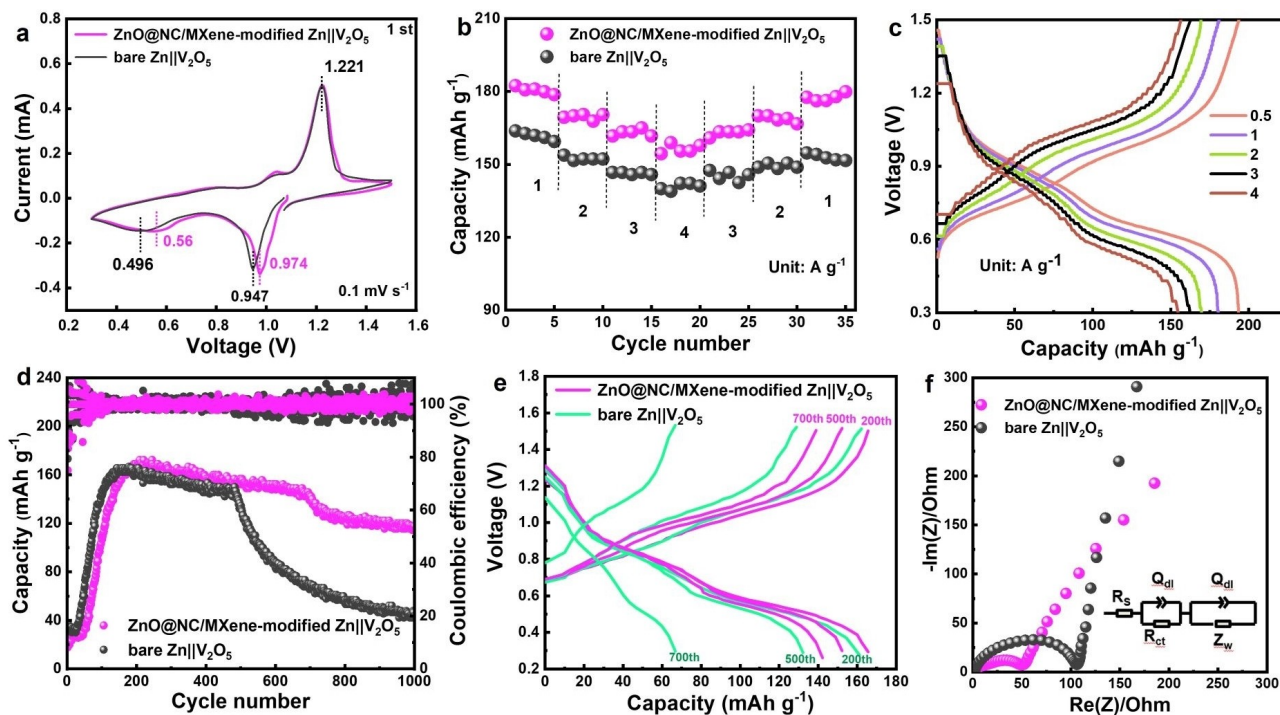
Figure 5. The performance comparison of bare $Zn||V_2O_5$ and ZnO@NC/MXene-modified $Zn||V_2O_5$ full cell. (a) CV curves. (b) Rate performance. (c) Galvanostatic charge–discharge curves at various current densities of ZnO@NC/MXene-modified $Zn||V_2O_5$ full cell. (d) Long-term cycling performance at 4 A g^{-1}. (e) Charge-discharge curves after activation at 4 A g^{-1}. (f) EIS spectra.

ZnO@NC/MXene interface layer, representing much improved charge transfer kinetics, which is contributed by the uniform electric field distribution and fast Zn adsorption and nucleation on the interface layer. Moreover, the Zn^{2+} diffusion coefficients are calculated based on the slope of Re(Z) to $\omega^{-0.5}$ in the low-frequency region (Figure S18).[49] The Zn^{2+} diffusion coefficient of the ZnO@NC/MXene-modified $Zn||V_2O_5$ cell (1.7×10^{-9} cm^2 s^{-1}) is higher than that of the bare $Zn||V_2O_5$ cell (1.1×10^{-9} cm^2 s^{-1}), demonstrating that the protective layer accelerates the Zn^{2+} transport and enhances the reaction kinetics.

Conclusions

In summary, the ZnO@NC/MXene composite was prepared by sintering a ZIF-8 MOF/Ti$_3$C$_2$T$_x$ MXene composite, and applied as a zincophilic and hydrophobic interface layer for protecting the Zn electrode. The nitrogen-doped carbon, ZnO, and MXene in the composite layer synergistically provide strong adsorption and uniform nucleation sites for Zn^{2+} ions as well as high conductivity, ensuring homogeneous Zn^{2+} deposition with fast kinetics. Moreover, the hydrophobic property of the layer limits side reactions such as HER and corrosion at the interface. The symmetrical cell assembled with ZnO@NC/MXene-modified Zn electrodes exhibits a remarkable cycle life of over 2600 h under the conditions of 1 mA cm^{-2} and 1 mAh cm^{-2}. The ZnO@NC/MXene-modified Zn||Cu asymmetrial cell shows an average CE of 99.37% for over 1000 cycles at 5 mA cm^{-2} and 1 mAh cm^{-2}.

Besides, the full cell based on the ZnO@NC/MXene-modified Zn anode and V$_2$O$_5$ cathode displays good cycle performance and rate capability, which presents a capacity retention of 71.1% after 1000 cycles at a current density of 4 A g^{-1}. This work not only provides a high-performance ZnO@NC/MXene material for stabilizng Zn electrode, but also highlights the superiority of the zincophilic and hydrophobic interface layer for enhancing the performance of AZIBs.

Supporting Information

Supporting Information is available from the Wiley Online Library or from the author.

Acknowledgements

Conflict of Interests

The authors declare no conflict of interest.

Data Availability Statement

The data that support the findings of this study are available from the corresponding author upon reasonable request.

[1] R. Shao, Z. Sun, L. Wang, J. Pan, L. Yi, Y. Zhang, J. Han, Z. Yao, J. Li, Z. Wen, S. Chen, S. L. Chou, D. L. Peng, Q. Zhang, *Angew. Chem. Int. Ed. Engl.* **2024**, *63*, e202320183.

[2] W. Shi, W. S. V. Lee, J. Xue, *ChemSusChem* **2021**, *14*, 1634–1658.

[3] H. Liu, Z. Xin, B. Cao, Z. Xu, B. Xu, Q. Zhu, J. L. Yang, B. Zhang, H. J. Fan, *Adv. Funct. Mater.* **2024**, *34*, 2309840.

[4] H. Liu, Z. J. Xu, B. Cao, Z. J. Xin, H. J. Lai, S. Gao, B. Xu, J. L. Yang, T. Xiao, B. Zhang, H. J. Fan, *Adv. Energy Mater.* doi: 10.1002/aenm.202400318.

[5] Z. Yang, C. Lv, W. Li, T. Wu, Q. Zhang, Y. Tang, M. Shao, H. Wang, *Small* **2022**, *18*, 2104148.

[6] Q. Li, A. Chen, D. Wang, Y. Zhao, X. Wang, X. Jin, B. Xiong, C. Zhi, *Nat. Commun.* **2022**, *13*, 3699.

[7] X. Zhang, J. P. Hu, N. Fu, W. B. Zhou, B. Liu, Q. Deng, X. W. Wu, *InfoMat* **2022**, *4*, e12306.

[8] J. Hao, B. Li, X. Li, X. Zeng, S. Zhang, F. Yang, S. Liu, D. Li, C. Wu, Z. Guo, *Adv. Mater.* **2020**, *32*, 2003021.

[9] J. Hao, X. Li, S. Zhang, F. Yang, X. Zeng, S. Zhang, G. Bo, C. Wang, Z. Guo, *Adv. Funct. Mater.* **2020**, *30*, 2001263.

[10] X.-Y. Fan, H. Yang, B. Feng, Y. Zhu, Y. Wu, R. Sun, L. Gou, J. Xie, D.-L. Li, Y.-L. Ding, *Chem. Eng. J.* **2022**, *445*, 136799.

[11] K. Chen, H. Guo, W. Li, Y. Wang, *ACS Appl. Mater. Interfaces* **2021**, *13*, 54990–54996.

[12] H. Li, L. Yang, S. Zhou, J. W. Li, Y. N. Chen, X. Y. Meng, D. M. Xu, C. Han, H. M. Duan, A. Q. Pan, *Adv. Funct. Mater.* **2024**, *34*, 2313859.

[13] H. Qin, W. Kuang, N. Hu, X. Zhong, D. Huang, F. Shen, Z. Wei, Y. Huang, J. Xu, H. He, *Adv. Funct. Mater.* **2022**, *32*, 2206695.

[14] K. Ouyang, F. Li, D. Ma, Y. Wang, S. Shen, M. Yang, J. Qiu, W. Wen, N. Zhao, H. Mi, P. Zhang, *ACS Energy Lett.* **2023**, *8*, 5229–5239.

[15] X. Zhang, J. Li, K. Qi, Y. Yang, D. Liu, T. Wang, S. Liang, B. Lu, Y. Zhu, J. Zhou, *Adv. Mater.* **2022**, *34*, 2205175.

[16] P. Wu, L. Xu, X. Xiao, X. Ye, Y. Meng, S. Liu, *Adv. Mater.* **2024**, *36*, 2306601.

[17] Y. Li, Q. Zhu, M. Xu, B. Zang, Y. Wang, B. Xu, *Adv. Funct. Mater.* **2023**, *33*, 2213416.

[18] J. Zhou, M. Xie, F. Wu, Y. Mei, Y. Hao, R. Huang, G. Wei, A. Liu, L. Li, R. Chen, *Adv. Mater.* **2021**, *33*, 2101649.

[19] C. Mao, Y. Chang, X. Zhao, X. Dong, Y. Geng, N. Zhang, L. Dai, X. Wu, L. Wang, Z. He, *J. Energy Chem.* **2022**, *75*, 135–153.

[20] J. Zhou, M. Xie, F. Wu, Y. Mei, Y. Hao, L. Li, R. Chen, *Adv. Mater.* **2022**, *34*, 2106897.

[21] P. Li, J. Ren, C. Li, J. Li, K. Zhang, T. Wu, B. Li, L. Wang, *Chem. Eng. J.* **2023**, *451*, 138769.

[22] H. He, H. Tong, X. Song, X. Song, J. Liu, *J. Mater. Chem. A* **2020**, *8*, 7836–7846.

[23] Y. Zhang, Y. Zhang, J. Deng, R. Xue, S. Yang, Y. Ma, Z. Wang, *Adv. Funct. Mater.* **2024**, *34*, 2310995.

[24] N. Zhang, S. Huang, Z. Yuan, J. Zhu, Z. Zhao, Z. Niu, *Angew. Chem. Int. Ed. Engl.* **2021**, *60*, 2861–2865.

[25] X. Zhu, X. Li, M. L. K. Essandoh, J. Tan, Z. Cao, X. Zhang, P. Dong, P. M. Ajayan, M. Ye, J. Shen, *Energy Storage Mater.* **2022**, *50*, 243–251.

[26] J. Ruan, D. Ma, K. Ouyang, S. Shen, M. Yang, Y. Wang, J. Zhao, H. Mi, P. Zhang, *Nano-Micro Lett.* **2023**, *15*, 37.

[27] Y. Li, D. Zhao, J. Cheng, Y. Lei, Z. Zhang, W. Zhang, Q. Zhu, *Chem. Eng. J.* **2023**, *452*, 139264.

[28] R. Zhang, S. Wen, N. Wang, K. Qin, E. Liu, C. Shi, N. Zhao, *Adv. Energy Mater.* **2018**, *8*, 1800914.

[29] F. Xie, H. Li, X. Wang, X. Zhi, D. Chao, K. Davey, S. Z. Qiao, *Adv. Energy Mater.* **2021**, *11*, 2003419.

[30] H. Liu, J. G. Wang, W. Hua, H. Sun, Y. Huyan, S. Tian, Z. Hou, J. Yang, C. Wei, F. Kang, *Adv. Sci.* **2021**, *8*, 2102612.

[31] Y. Meng, M. Wang, J. Xu, K. Xu, K. Zhang, Z. Xie, Z. Zhu, W. Wang, P. Gao, X. Li, W. Chen, *Angew. Chem. Int. Ed. Engl.* **2023**, *62*, e202308454.

[32] W. Deng, N. Zhang, X. Wang, *Chem. Eng. J.* **2022**, *432*, 134378.

[33] H. Chen, Y. Wang, S. Zhang, Y. He, L. Hou, C. Yuan, *Chem. Eng. J.* **2024**, *479*, 147422.

[34] Q. Xu, W. Zhou, T. Xin, Z. Zheng, X. Yuan, J. Liu, *J. Mater. Chem. A* **2022**, *10*, 12247–12257.

[35] Y. Wei, P. Zhang, R. A. Soomro, Q. Zhu, B. Xu, *Adv. Mater.* **2021**, *33*, 2103148.

[36] Z. Xu, Z. Zhang, X. Li, Q. Dong, Y. Qian, Z. Hou, *ACS Appl. Mater. Interfaces* **2023**, *15*, 15574–15584.

[37] H. Fan, M. Li, E. Wang, *Nano Energy* **2022**, *103*, 107751.

[38] Y. Xu, Y. Gao, S. Xiang, J. Zhou, F. Liu, Z. Li, H. Zhou, *Desalination* **2023**, *546*, 116220.

[39] C. Guo, Q. Wang, J. He, C. Wu, K. Xie, Y. Liu, W. Zhang, H. Cheng, H. Hu, C. Wang, *J. Phys. Chem. Lett.* **2020**, *11*, 905–912.

[40] B. Cao, H. Liu, X. Zhang, P. Zhang, Q. Zhu, H. Du, L. Wang, R. Zhang, B. Xu, *Nano-Micro Lett.* **2021**, *13*, 202.

[41] C. Zhao, Y. Lin, Q. Lin, Q. Liu, Y. Liu, Z. Liu, A. Ying, *Energy Storage Mater.* **2023**, *58*, 332–343.

[42] M.-C. Liu, C.-Y. Tian, D.-T. Zhang, Y.-S. Zhang, B.-M. Zhang, Y.-Y. Wang, C.-Y. Li, M.-J. Liu, B. Gu, K. Zhao, L.-B. Kong, Y.-L. Chueh, *Nano Energy* **2022**, *103*, 107805.

[43] X. Chen, W. Li, D. Reed, X. Li, X. Liu, *Electrochem. Energy Rev.* **2023**, *6*, 33.

[44] H. He, H. Qin, J. Wu, X. Chen, R. Huang, F. Shen, Z. Wu, G. Chen, S. Yin, J. Liu, *Energy Storage Mater.* **2021**, *43*, 317–336.

[45] W. He, T. Gu, X. Xu, S. Zuo, J. Shen, J. Liu, M. Zhu, *ACS Appl. Mater. Interfaces* **2022**, *14*, 40031–40042.

[46] P. X. Sun, Z. Cao, Y. X. Zeng, W. W. Xie, N. W. Li, D. Luan, S. Yang, L. Yu, X. W. D. Lou, *Angew. Chem. Int. Ed. Engl.* **2022**, *61*, e202115649.

[47] Y. Wang, S. Zhang, Y. Zhang, F. Chu, L. Hou, C. Yuan, *Electrochim. Acta* **2024**, *475*, 143623.

[48] N. Zhang, Y. Dong, M. Jia, X. Bian, Y. Wang, M. Qiu, J. Xu, Y. Liu, L. Jiao, F. Cheng, *ACS Energy Lett.* **2018**, *3*, 1366–1372.

[49] X. Y. Zhou, P. H. Cao, A. R. Wei, A. T. Zou, H. Ye, W. P. Liu, J. J. Tang, J. Yang, *ACS Appl. Mater. Interfaces* **2021**, *13*, 8181–8190.